Electronic Supplementary Material (ESI) for Dalton Transactions.

Supramolecular adducts based on weak interactions between the trimeric Lewis acid complex (perfluoro-*ortho*-phenylene)mercury and polypnictogen complexes

Martin Fleischmann,[a] James S. Jones,[b] Gábor Balázs,[a] François P. Gabbaï[b]* and Manfred Scheer[a]*

a) Institut für Anorganische Chemie, Universität Regensburg, 93040 Regensburg, Germany, manfred.scheer@chemie.uni-regensburg.de Fax: (+49) 941-943-4439.

b) Department of Chemistry, Texas A&M University, College Station, Texas 77843-3255, USA.

Contents

1 Experimental section

1.1 General considerations

Extreme precaution was used working with Hg containing compounds to not get in contacts with solid samples or solutions by wearing protective gloves, goggles and lab coats. All experiments were performed under an atmosphere of dry argon or nitrogen using standard Schlenk and drybox techniques. Solvents were freshly distilled under nitrogen from CaH_2 (CH_2Cl_2, CD_2Cl_2), Solution NMR spectra were recorded on a Bruker Avance 300 MHz NMR spectrometer (^1H: 300.132 MHz, ^{31}P: 121.495 MHz, ^{13}C: 75.468 MHz, ^{19}F: 282.404 MHz). The chemical shifts δ are presented in parts per million (ppm). The following samples were used for external reference: TMS (^1H, ^{13}C), $CFCl_3$ (^{19}F), H_3PO_4 85 % (^{31}P). IR spectra were recorded on a VARIAN FTS-800 FT-IR spectrometer. FD-MS spectra were measured on a Finnigan MAT 95 mass spectrometer. Elemental analyses were recorded on an Elementar Vario EL III apparatus by the microanalytical laboratory of the University of Regensburg. The solid substances were grinded together with dried KBr and pressed to pellets. The starting materials **1, 2, 3a-d, 4** were prepared according to the literature procedure, while a new synthesis for **3c** is described below.[1,2,3,4,5]

1.2 Synthetic procedures

Preparation of **3c**: 1.14 g (4.04 mmol, 1eq.) $[(Me_3Si)_2CHSbH_2]$[6] and 1.05 g (4.04 mmol, 1eq.) $[CpMo(CO)_3Me]$ were dissolved in 15 mL xylene and stirred under reflux for 3 h. After filtration and concentration the red solution was stored at -28°C to give red crystals of **3**. The crystals were isolated by filtration, the mother liquor concentrated and stored at -28°C to give two additional crops of **3**. Yield: 0.776 g (57%). For analytical data see ref. [3].

Preparation of [(**1**)●(**2**)]: 50 mg **1** (0.05 mmol, 1eq.) and 15 mg **2** (0.05 mmol, 1eq.) were dissolved together in 10 mL CH_2Cl_2 and stirred at room temperature for 1 h. After filtration and concentration of the solution the adduct [(**1**)●(**2**)] crystallizes as clear yellow blocks in the course of one day. Yield: 52 mg (80%). NMR spectra (300 MHz, CD_2Cl_2): ^1H: δ/ppm = 5.29 (s, Cp); $^{19}F\{^1H\}$: δ/ppm = –120.6 (m, *o*-F), –155.2 (m, *p*-F); $^{31}P\{^1H\}$: δ/ppm = –349.5 (s, P_3). IR (KBr): v/cm^{-1} = 3119 (vw), 2022 (vs), 1962 (vs), 1616 (m), 1583 (m), 1472 (vs), 1418 (vs), 1356 (w), 1321 (w), 1306 (w), 1288 (m), 1251 (w), 1087 (s), 1004 (s), 814 (m), 771 (w), 732 (w). FD-MS (CH_2Cl_2): *m*/*z*(%) 312(18) [**2**], 1047.0(100) [**1**]. Elemental analysis (%) calc. for [(**1**)●(**2**)](CH_2Cl_2): C 21.67, H 0.49; found: C 21.82, H 0.53.

Preparation of [(**1**)●(**3a**)]: 105 mg **1** (0.1 mmol, 1eq.) and 50 mg **3a** (0.1 mmol, 1eq.) were dissolved together in 10 mL CH_2Cl_2 and stirred at room temperature for 1 h. After filtration and concentration of the solution the adduct [(**1**)●(**3a**)] crystallizes as clear orange blocks in the course of one day. Yield: 115 mg (75%). NMR spectra (300 MHz, CD_2Cl_2): ^1H: δ/ppm = 5.09 (s, Cp); $^{19}F\{^1H\}$: δ/ppm = –119.9 (m, *o*-F), –155.6 (m, *p*-F); $^{31}P\{^1H\}$: δ/ppm = –55.7 (s, P_2). IR (KBr): v/cm^{-1} = 3120 (vw), 2011 (vs), 1955 (vs), 1944 (vs), 1878 (vs), 1614 (w), 1583 (w), 1471 (vs), 1418 (vs), 1356 (w), 1321 (w), 1305 (w), 1286 (m), 1248 (w), 1087 (s), 1004 (s), 812 (m), 770 (w). FD-MS (CH_2Cl_2): *m*/*z*(%) 497.1(100) [**3a**], 1047.0(37) [**1**]. Elemental analysis (%) calc. for [(**1**)●(**3a**)]$(CH_2Cl_2)_{0.5}$: C 24.64, H 0.70; found: C 24.78, H 0.74.

Preparation of [(**1**)●(**3b**)]: 105 mg **1** (0.1 mmol, 1eq.) and 58 mg **3b** (0.1 mmol, 1eq.) were dissolved together in 10 mL CH_2Cl_2 and stirred at room temperature for 1 h. After filtration and concentration of the solution the adduct [(**1**)●(**3b**)] crystallizes as clear light red blocks in the course of a few days. Yield: 120 mg (74%). NMR spectra (300 MHz, CD_2Cl_2): ^1H: δ/ppm = 5.09 (s, Cp); $^{19}F\{^1H\}$: δ/ppm = –120.4 (m, *o*-F), –155.4 (m, *p*-F). IR (KBr): v/cm^{-1} = 3118 (vw), 3104 (vw), 1998 (vs), 1975 (vs), 1926 (vs), 1874 (vs), 1616 (w), 1583 (w), 1472 (vs), 1418 (vs), 1356 (w), 1321 (w), 1306 (w), 1287 (m), 1251 (w), 1088 (s), 1005 (s), 814 (m), 771 (w). FD-MS (CH_2Cl_2): *m*/*z*(%) 585.9(88) [**3b**], 1047.0(100) [**1**]. Elemental analysis (%) calc. for [(**1**)●(**3b**)]: C 23.58, H 0.62; found: C 23.59, H 0.64.

Preparation of [(**1**)•(**3c**)] and [(**1**)$_2$•(**3c**)]: 105 mg **1** (0.1 mmol) and 68 mg **3c** (0.1 mmol) were dissolved together in 10 mL CH_2Cl_2 forming a dark red solution and stirred at room temperature for 30 min. After filtration and concentration of the solution the formation of orange [(**1**)•(**3c**)] and red [(**1**)$_2$•(**3c**)] crystals is observed from the same solution. The mother liquor was decanted off and the crystals dried in vacuum. Yield: 98 mg (mixture). NMR spectra (300 MHz, CD_2Cl_2): ^{1}H: δ/ppm = 5.03 (s, Cp); ^{19}F{^{1}H}: δ/ppm = –120.7 (m, *o*-F), –155.3 (m, *p*-F). IR (KBr): ν/cm^{-1} = 3121 (vw), 2055 (w), 2004 (w), 1967 (s), 1931 (vs), 1893 (vs), 1839 (s), 1615 (w), 1583 (w), 1471 (vs), 1418 (vs), 1357 (vw), 1321 (w), 1305 (vw), 1288 (m), 1250 (w), 1083 (s), 1005 (s), 837 (vw), 815 (m), 770 (w). FD-MS (CH_2Cl_2): *m*/*z*(%) 678.9(87) [**3c**], 1045.0(100) [**1**].

Preparation of [(**1**)•(**3d**)$_2$]: A dark red CH_2Cl_2 solution of **1** and **3d** (~0.1 mmol) was stirred for 30 min. After filtration and subsequent concentration the formation of different black and white crystals was observed. The coexistence of pure **1**, pure **3d** and the adduct [(**1**)•(**3d**)$_2$] was determined by single crystal X-ray diffraction analysis. The adduct [(**1**)•(**3d**)$_2$] could only be obtained in mixtures and was solely characterized by X-ray structure determination.

1.3 NMR study of 1 and 3a in different ratios

The described adducts are based on weak interactions in the solid state. During our study, an upfield shift of the P_2 complex **3a** has been observed when crystals of the adduct [(**1**)•(**3a**)] were dissolved in CD_2Cl_2. This suggests, that the interactions are also present in solution. Combining the reactants in different molar ratios (see Figure S1) results in a continuous upfield shift of the P_2 complex **3a** with increasing amount of **1**. Attempts to extract the equilibrium constant from this series of spectra by using a modified Benesi-Hildebrand equation for NMR studies failed.[7] The exact nature of the species in solution cannot be determined. Due to the geometry of the reactants several species (1:1, 1:2 or 2:1) may be present in the underlying equilibrium. The dynamic processes are fast on the NMR timescale and only one singlet can be observed.

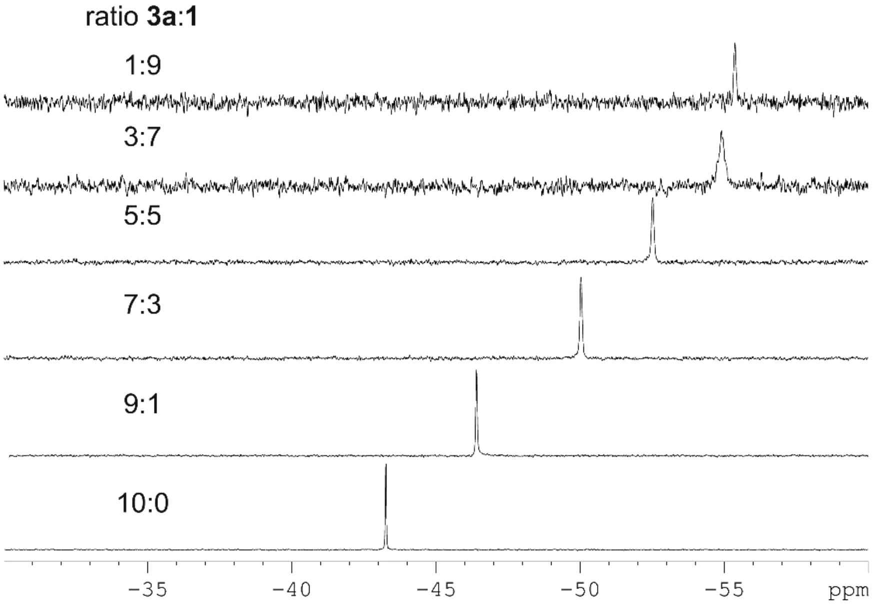

Figure S1. ^{31}P{^{1}H} NMR spectra of different mixtures of **3a** and **1** in varying molar ratios in CD_2Cl_2 solution.

2 X-ray crystallography

All diffraction experiments were performed at 123 K except the one for **3c** which was performed at 173 K. The data sets were either collected on Rigaku (former: Agilent Technologies or Oxford Diffraction) Gemini R Ultra diffractometer with MoK_α or on a SuperNova diffractometer with either Cu$K\alpha$ or MoK_α or on a STOE IPDS diffractometer with MoK_α radiation. Crystallographic data together with the details of the experiments are given in the Tables S1-S3. All crystal preparations were performed under mineral oil. The structure solution and refinement was done with ShelX.[8] The H atoms were calculated geometrically and a riding model was used during the refinement process. Graphical material was created with Olex2.[9]

CIF files with comprehensive information on the details of the diffraction experiments and full tables of bond lengths and angles for **1-4** are deposited in Cambridge Crystallographic Data Centre under the deposition codes CCDC-1486626 - CCDC-1486635, respectively. Crystallographic data and details of the diffraction experiments are given in Tables S1-S3.

Table S1. Crystallographic details of [**1•2**], [**1•3a**], [**1**$_2$**•3c**] and [**1•3c**].

Identification code	[**1•2**]	[**1•3a**]	[**1**$_2$**•3c**]	[**1•3c**]
formula	$C_{26}H_7Cl_2F_{12}$ $Hg_3MoO_2P_3$	$C_{66}H_{24}Cl_4F_{24}$ $Hg_6Mo_4O_8P_4$	$C_{50}H_{10}F_{24}$ $Hg_6Mo_2O_4Sb_2$	$C_{33}H_{12}Cl_2F_{12}$ $Hg_3Mo_2O_4Sb_2$
weight [g·mol^{-1}]	1440.84	3253.83	2769.50	1808.48
Temperature [K]	123(1)	123(1)	123(1)	123(1)
crystal system	triclinic	triclinic	monoclinic	triclinic
space group	*P*–1	*P*–1	*P*2/*n*	*P*–1
a [Å]	11.1294(2)	12.8301(7)	11.0707(2)	12.4435(3)
b [Å]	11.5500(2)	12.8847(6)	7.4335(2)	13.3321(3)
c [Å]	14.1425(3)	23.5633(12)	33.0847(8)	14.0134(4)
α [°]	114.075(2)	92.367(4)	90	81.649(2)
β [°]	104.952(2)	100.819(4)	95.819(2)	71.018(2)
γ [°]	91.314(2)	94.276(4)	90	63.354(2)
V [Å^3]	1586.58(6)	3809.3(3)	2708.64(11)	1964.90(9)
Z	2	2	2	2
ρ_{calc} [g·cm^{-3}]	3.016	2.837	3.396	3.057
μ [mm^{-1}]	32.529	13.011	18.488	13.877
F(000)	1296.0	2952.0	2448.0	1620.0
crystal size [mm^3]	0.30 × 0.25 × 0.04	0.17 × 0.12 × 0.06	0.08 × 0.06 × 0.03	0.12 × 0.08 × 0.04
diffractometer	SuperNova	Gemini R ultra	Gemini R ultra	Gemini R ultra
absorption correction	gaussian	analytical	gaussian	gaussian
T_{min}/T_{max}	0.016 / 0.357	0.267 / 0.582	0.359 / 0.614	0.331 / 0.621
radiation [Å]	CuK_α	MoK_α	MoK_α	MoK_α
2 Θ range [°]	8.31 to 134.124	5.65 to 60.372	6.796 to 59.798	5.574 to 54.206
completeness	0.988	0.998	0.974	0.999
reflns collected/unique	59642 / 5661	58978 / 19714	15226 / 6532	19426 / 8644
R_{int}/R_{sigma}	0.0628 / 0.0198	0.0356 / 0.0383	0.0287 / 0.0439	0.0321 / 0.0744
data/restraints/ parameters	5661 / 6 / 442	19714 / 12 / 1089	6532 / 0 / 397	8644 / 12 / 550
GOF on F^2	1.249	1.039	0.883	0.813
R_1/wR_2 [I ≥ 2σ(I)]	0.0264 / 0.0731	0.0247 / 0.0479	0.0216 /0.0367	0.0297 / 0.0462
R_1/wR_2 [all data]	0.0269 / 0.0743	0.0309 / 0.0505	0.0322 / 0.0377	0.0516 / 0.0482
max/min $\Delta\rho$ [e·Å^{-3}]	0.98 / –2.10	0.94 / –0.98	1.01 / –1.02	2.14 / –1.64

Table S2. Crystallographic details of [**1•3b**], [**1•3d$_2$**] and **3d**.

Identification code	[**1•3b**]	[**1•3d$_2$**]	**3d**
formula	$C_{33}H_{12}As_2Cl_2F_{12}Hg_3Mo_2O_4$	$C_{48}H_{24}Bi_4Cl_4F_{12}Hg_3Mo_4O_8$	$C_{14}H_{10}Bi_2Mo_2O_4$
weight [g·mol^{-1}]	1714.82	2919.92	852.06
Temperature [K]	123(1)	123(1)	123(1)
crystal system	triclinic	triclinic	monoclinic
space group	*P*–1	*P*–1	*C*2/*c*
a [Å]	12.7941(3)	13.5154(2)	16.5867(11)
b [Å]	13.4465(4)	14.6000(2)	7.6677(4)
c [Å]	13.5405(5)	17.6515(3)	14.3800(8)
α [°]	60.580(3)	111.087(2)	90
β [°]	71.346(3)	103.308(2)	115.265(7)
γ [°]	69.203(2)	104.4830(10)	90
V [Å^3]	1866.34(12)	2942.32(9)	1653.93(19)
Z	2	2	4
ρ_{calc} [g·cm^{-3}]	3.051	3.296	3.422
μ [mm^{-1}]	14.952	20.797	22.709
F(000)	1548.0	2584.0	1504.0
crystal size [mm^3]	0.08 × 0.04 × 0.02	0.13 × 0.08 × 0.04	0.23 × 0.19 × 0.04
diffractometer	SuperNova	Gemini R ultra	Gemini R ultra
absorption correction	gaussian	gaussian	gaussian
T_{min}/T_{max}	0.528 / 0.801	0.203 / 0.520	0.055 / 0.435
radiation [Å]	MoK_α	MoK_α	MoK_α
2 Θ range [°]	6.06 to 59.31	5.41 to 54.206	6.266 to 54.188
completeness	0.991	0.999	0.994
reflns collected/unique	16291 / 8975	74152 / 12972	3154 / 1812
R_{int}/R_{sigma}	0.0337 / 0.0685	0.0479 / 0.0539	0.0376 / 0.0665
data/restraints/parameters	8975 / 0 / 523	12972 / 0 / 748	1812 / 0 / 100
GOF on F^2	0.823	0.834	0.925
R_1/wR_2 [I ≥ 2σ(I)]	0.0262 / 0.0400	0.0230 / 0.0386	0.0331 / 0.0667
R_1/wR_2 [all data]	0.0425 / 0.0412	0.0359 / 0.0395	0.0438 / 0.0685
max/min Δρ [e·Å^{-3}]	1.17 / –1.27	1.49 / –1.75	1.55 / –1.52

Table S3. Crystallographic details of **3c**, **4** and [**1•5**].

Identification code	**3c**	**4**	[**1•5**]
formula	$C_{14}H_{10}Mo_2O_4Sb_2$	$C_{24}H_{15}BiMo_3O_9$	$C_{59}H_{26}As_5Cl_6Cr_4F_{24}Hg_6$
weight [g·mol^{-1}]	677.60	944.16	3189.64
Temperature [K]	173(1)	123(1)	123(1)
crystal system	trigonal	trigonal	monoclinic
space group	*P*3$_2$21	P31c	C2/c
a [Å]	8.6935(4)	14.8747(6)	19.18520(10)
b [Å]	8.6935(4)	14.8747(6)	19.78690(10)
c [Å]	19.7356(14)	7.4995(4)	18.72880(10)
α [°]	90.00	90	90
β [°]	90.00	90	99.0540(10)
γ [°]	120.00	120	90
V [Å^3]	1291.73(17)	1437.01(14)	7021.16(7)
Z	3	2	4
ρ_{calc} [g·cm^{-3}]	2.613	2.182	3.017
μ [mm^{-1}]	4.537	7.429	33.451
F(000)	936.0	880	5756.0
crystal size [mm^3]	0.26 × 0.16 × 0.16	0.27 × 0.02 × 0.02	0.24 × 0.08 × 0.05
diffractometer	STOE IPDS	SuperNova (Mo)	Gemini R ultra
absorption correction	numerical	gaussian	gaussian
T_{min}/T_{max}	0.4495 / 0.5920	0.243 / 0.814	0.030 / 0.340
radiation [Å]	MoK_α	MoK_α	CuK_α
2 Θ range [°]	5.42 to 51.78	6.286 to 52.714	6.458 to 133.09
completeness	0.996	0.976	0.972
reflns collected/unique	10028 / 1686	5998 / 1680	21971 / 6190
R_{int}/R_{sigma}	0.0236 / 0.0133	0.1451 / 0.1541	0.0375 / 0.0291
data/restraints/parameters	1686 / 0 / 100	1680 / 1 / 112	6190 / 0 / 483
GOF on F^2	1.138	0.92	1.031
R_1/wR_2 [I ≥ 2σ(I)]	0.0196 / 0.0519	0.0686 / 0.1526	0.0254 / 0.0578
R_1/wR_2 [all data]	0.0207 / 0.0521	0.1111 / 0.1620	0.0284 / 0.0588
max/min Δρ [e·Å^{-3}]	1.07 / –0.48	2.32 / –1.96	1.60 / –1.71
Flack parameter	0.00(3)	0.00(2)	

3 DFT calculations

3.1 Electrostatic potential maps

In order to aid in the rationalization of the observed structural trends for the adducts of **3a-3d** and **1**, their constituent compounds were optimized by density functional theory (DFT) methods. The large computed HOMO-LUMO gaps between **1** and **3a-d** of 3.06, 3.00, 2.88, and 2.74 eV, respectively, suggest that orbital-based interactions are not likely to be dominant within the pnictogen-mercury bonding found in these adducts. Instead, electrostatic and dispersion forces are likely to factor strongly in the stabilization of the observed structures. In order to probe the potential role of electrostatic forces in the observed adducts, we inspected the electrostatic potential maps of the constituent complexes.

These DFT calculations (full geometry optimizations) were carried out on compounds **1** and **3a-d** starting from their crystal structure geometries observed in their respective adducts using the Gaussian09 program (B3LYP,[10] with cc-pVTZ[11] for H, C, O, and F; and aug-cc-pVTZ for P, As, Sb, and Bi;[12] Stuttgart relativistic small effective core potentials for Sb and Bi[13]). Frequency calculations were carried out on the optimized geometries, showing no imaginary frequencies.

3.2 QTAIM analysis of Mo_2E_2 adducts with 1

QTAIM[14] calculations were performed using the AIMAll program[15] at the crystal structure geometries of adducts [(**1**)•(**3a**)], [(**1**)•(**3b**)], [(**1**)$_2$•(**3c**)], [(**1**)•(**3c**)], and [(**1**)•(**3d**)$_2$] using wavefunctions derived from DFT single point energy calculations performed using the Gaussian 09 program[16] (Functional: B3LYP,[10] mixed basis sets: H, C: 6-31G; O, F: 6-31(d');[17] P, As, Mo, Sb, Bi, Hg: cc-pVTZ,[10,11,18] with Stuttgart relativistic small core effective core potentials (ECPs)).[11,19,20] In contrast to what would be expected from the η^5 coordination mode, QTAIM analysis finds that 1-2 carbons of the cyclopentadienyl ligands of the Mo_2E_2 complexes do not share bond critical points (BCPs) with their proximal molybdenum centers in all cases. Additionally, while the QTAIM analysis of Mo_2P_2 complex in [(**1**)•(**3a**)] does not find a shared BCP between the two Mo centers, weak BCPs are found between the Mo centers in [(**1**)•(**3b**)], [(**1**)$_2$•(**3c**)], [(**1**)•(**3c**)], and [(**1**)•(**3d**)$_2$]. These inconsistencies persisted through changes in functional and basis set, as well as attempts to partially optimize the Mo_2E_2 complex within the adducts by DFT methods.

Optimization of the free Mo_2E_2 complexes by DFT methods at the same level of theory used for the single point calculations resulted in similar issues in observed QTAIM connectivity in most cases. Only in the case of **3a** did each carbon atom of the cyclopentadienyl ligands in the optimized structure feature a shared BCP with its proximal molybdenum center. Inspection of the features of the electron density distribution function (ρ(r)) of both the free Mo_2E_2 complexes and the Mo_2E_2 complexes within the adducts found that optimization of the Mo_2E_2 complex and in some cases the changing connectivity of the Mo atom results in minimal perturbation of the Mo_2E_2 core (Figure 2-Figure 5, Table 4-Table 7).

The observed inconsistencies in connectivity may be attributed the strongly delocalized nature of the bonding within the Mo_2E_2 cores. Indeed, similar difficulties have been encountered in the investigation of M-M interactions within complexes containing ligands that directly bridge the two metal centers.[21,22,23]

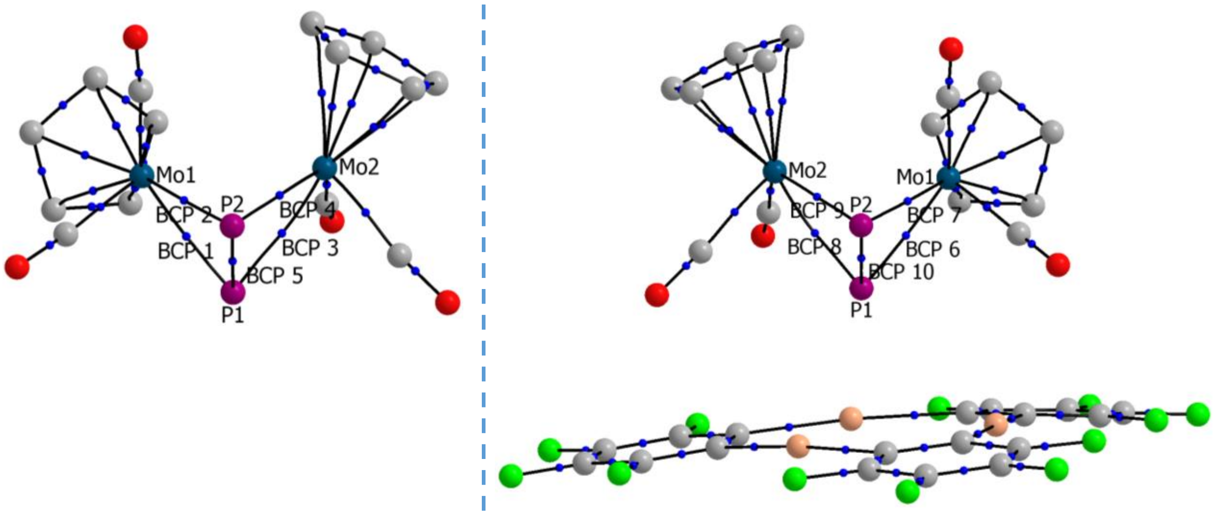

Figure 2. (Left) DFT-optimized electronic structure of **3a**. (Right) Electronic structure of [(**1**)•(**3a**)] at the observed crystal geometry. Bond critical points located *via* QTAIM analysis are shown as blue dots, with selected bond critical points of the Mo_2Sb_2 fragments labeled. Hydrogen atoms and bond critical points featuring *ρ*(r) values less than 0.006 e Å^{-3} are their corresponding bond paths are omitted for clarity.

Table 4. Features of the electron density distribution function (*ρ*(r)) at selected bond critical points of the Mo_2P_2 fragments in the structures of **3a** (white) and [(**1**)•(**3a**)] (grey).

BCP no. (A-B)	$d_{A\text{-}BCP}$ (Å)	$d_{B\text{-}BCP}$ (Å)	$\rho(r_{BCP})$ (e Å^{-3})	$\nabla^2\rho(r_{BCP})$ (e Å^{-5})	H_{BCP} (Hartree Å^{-3})	ε	*δ*(A,B)	$\oint_{A\cap B}\rho(r)$ (e Å^{-1})
1 (Mo1-P1)	1.265	1.232	0.518	1.19	-0.18	0.11	0.81	2.21
2 (Mo1-P2)	1.317	1.289	0.422	1.17	-0.13	0.42	0.64	1.34
3 (Mo2-P1)	1.317	1.289	0.422	1.17	-0.13	0.42	0.64	1.34
4 (Mo2-P2)	1.265	1.232	0.518	1.19	-0.18	0.11	0.81	2.21
5 (P1-P2)	1.045	1.045	0.878	-3.35	-0.53	0.13	1.40	2.82
6 (Mo1-P1)	1.244	1.207	0.553	1.39	-0.20	0.11	0.80	2.33
7 (Mo1-P2)	1.299	1.262	0.458	1.16	-0.15	0.31	0.64	1.48
8 (Mo2-P1)	1.282	1.255	0.469	1.34	-0.15	0.30	0.65	1.46
9 (Mo2-P2)	1.250	1.209	0.553	1.25	-0.20	0.10	0.81	2.34
10 (P1-P2)	1.056	1.040	0.861	-3.05	-0.51	0.13	1.30	2.90

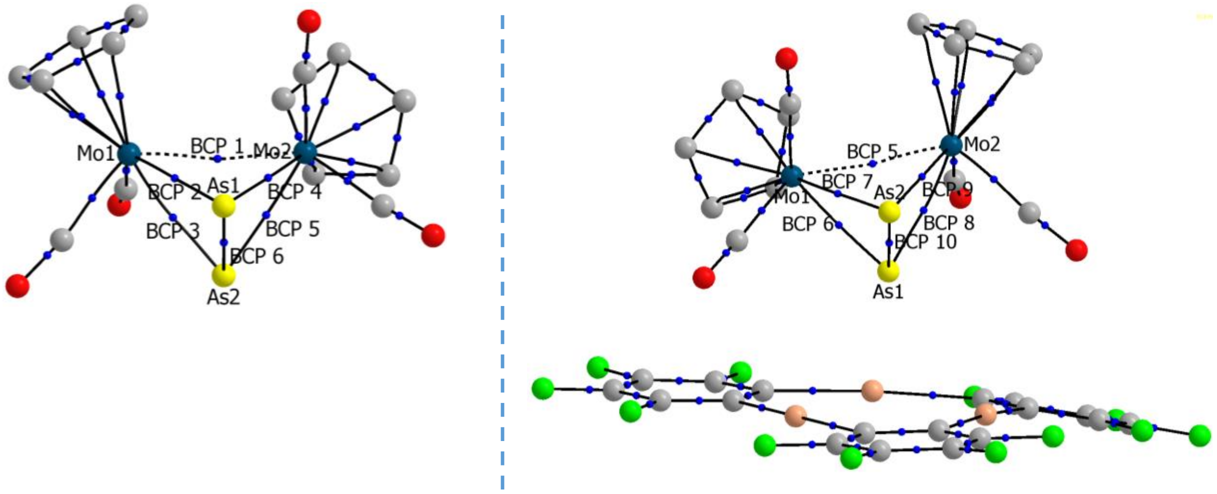

Figure 3. (Left) DFT-optimized electronic structure of **3b**. (Right) Electronic structure of [(**1**)•(**3b**)] at the observed crystal geometry. Bond critical points located *via* QTAIM analysis are shown as blue dots, with selected bond critical points of the Mo$_2$Sb$_2$ fragments labeled. Hydrogen atoms and bond critical points featuring ρ(r) values less than 0.006 e Å^{-3} are their corresponding bond paths are omitted for clarity.

Table 5. Features of the electron density distribution function (ρ(r)) at selected bond critical points of the Mo$_2$As$_2$ fragments in the structures of **3b** (white) and [(**1**)•(**3b**)] (grey).

BCP no. (A-B)	$d_{A\text{-}BCP}$ (Å)	$d_{B\text{-}BCP}$ (Å)	$\rho(r_{BCP})$ (e Å^{-3})	$\nabla^2 \rho(r_{BCP})$ (e Å^{-5})	H_{BCP} (Hartree Å^{-3})	ε	δ(A,B)	$\oint_{A\cap B}\rho(r)$ (e Å^{-1})
1 (Mo1-Mo2)	1.565	1.565	0.235	0.63	-0.05	1.34	0.42	N/A^a
2 (Mo1-As1)	1.306	1.303	0.453	1.03	-0.14	0.15	0.80	1.45
3 (Mo1-As2)	1.367	1.356	0.369	0.92	-0.10	0.25	0.62	1.27
4 (Mo2-As1)	1.367	1.356	0.369	0.92	-0.10	0.25	0.62	1.27
5 (Mo2-As2)	1.306	1.303	0.453	1.03	-0.14	0.15	0.80	1.44
6 (As1-As2)	1.161	1.161	0.645	-0.49	-0.29	0.15	1.30	1.79
5 (Mo1-Mo2)	1.527	1.518	0.264	0.66	-0.06	0.40	0.44	N/A^a
6 (Mo1-As1)	1.276	1.273	0.493	1.30	-0.16	0.17	0.78	N/A^a
7 (Mo1-As2)	1.344	1.331	0.400	0.97	-0.12	0.19	0.63	N/A^a
8 (Mo2-As1)	1.329	1.319	0.413	1.06	-0.12	0.16	0.61	N/A^a
9 (Mo2-As2)	1.295	1.287	0.475	1.07	-0.16	0.14	0.78	N/A^a
10 (As1-As2)	1.165	1.152	0.647	-0.39	-0.29	0.16	1.20	N/A^a

a: Due to the necessity to integrate the relevant atomic basins using the ‘Promega’ algorithm in AIMAll, the $\oint_{A\cap B}\rho(r_{BCP})$ value could not be determined.

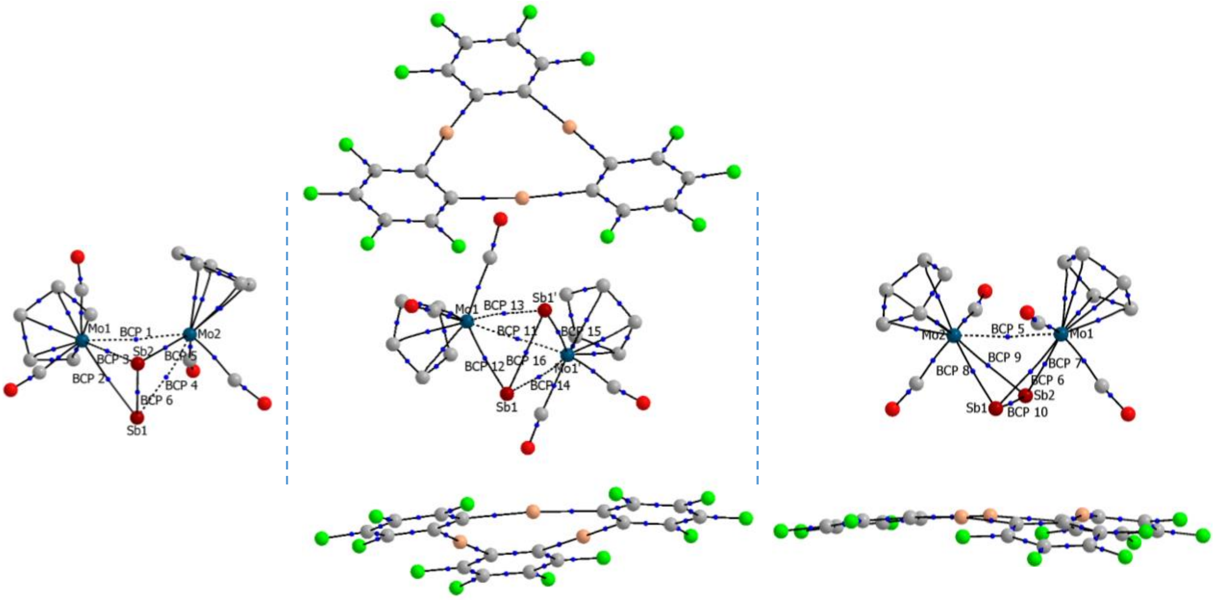

Figure 4. (Left) DFT-optimized electronic structure of **3c**. (Middle) Electronic structure of [(**1**)$_2$•(**3c**)] at the observed crystal geometry. (Right) Electronic structure of [(**1**)•(**3c**)] at the observed crystal geometry. Bond critical points located *via* QTAIM analysis are shown as blue dots, with selected bond critical points of the Mo_2Sb_2 fragments labeled. Hydrogen atoms and bond critical points featuring ρ(r) values less than 0.006 e Å^{-3} are their corresponding bond paths are omitted for clarity.

Table 6. Features of the electron density distribution function (ρ(r)) at selected bond critical points of the Mo_2Sb_2 fragments in the structures of **3c** (white), [(**1**)$_2$•(**3c**)] (grey), and [(**1**) •(**3c**)] (dark grey).

BCP no. (A-B)	$d_{A\text{-}BCP}$ (Å)	$d_{B\text{-}BCP}$ (Å)	$\rho(r_{BCP})$ (e Å^{-3})	$\nabla^2 \rho(r_{BCP})$ (e Å^{-5})	H_{BCP} (Hartree Å^{-3})	ε	δ(A,B)	$\oint_{A\cap B}\rho(r)$ (e Å^{-1})
1 (Mo1-Mo2)	1.600	1.600	0.215	0.38	-0.04	0.06	0.41	N/A^{a}
2 (Mo1-Sb1)	1.382	1.435	0.373	0.62	-0.11	0.19	0.78	1.29
3 (Mo1-Sb2)	1.451	1.481	0.306	0.57	-0.08	0.14	0.59	1.21
4 (Mo2-Sb1)	1.451	1.481	0.351	0.57	-0.08	0.14	0.59	1.21
5 (Mo2-Sb2)	1.382	1.435	0.373	0.62	-0.11	0.19	0.78	1.29
6 (Mo1-Mo2)	1.350	1.350	0.445	0.29	-0.16	0.20	1.23	1.43
11 (Mo1-Mo1')	1.567	1.567	0.238	0.44	-0.05	0.04	0.43	N/A^{a}
12 (Mo1-Sb1)	1.358	1.404	0.401	0.74	-0.13	0.19	0.77	1.38
13 (Mo1-Sb1')	1.421	1.448	0.334	0.66	-0.09	0.19	0.60	1.31
14 (Mo1'-Sb1)	1.421	1.448	0.334	0.66	-0.09	0.19	0.60	1.31
15 (Mo1'-Sb1')	1.358	1.404	0.401	0.74	-0.13	0.19	0.77	1.37
16 (Sb1-Sb1')	1.344	1.344	0.450	0.38	-0.16	0.22	1.14	1.41
5 (Mo1-Mo2)	1.561	1.561	0.242	0.43	-0.05	0.06	0.42	N/A^{a}
6 (Mo1-Sb1)	1.414	1.444	0.341	0.63	-0.10	0.07	0.59	1.30
7 (Mo1-Sb2)	1.361	1.405	0.399	0.74	-0.12	0.19	0.76	1.34
8 (Mo2-Sb1)	1.351	1.411	0.399	0.79	-0.12	0.20	0.76	1.32
9 (Mo2-Sb2)	1.418	1.437	0.346	0.59	-0.10	0.09	0.60	1.36
10 (Sb1-Sb2)	1.348	1.345	0.444	0.42	-0.16	0.23	1.12	1.56

a: Due to the necessity to integrate the relevant atomic basins using the 'Promega' algorithm in AIMAll, the $\oint_{A\cap B}\rho(r_{BCP})$ value could not be determined.

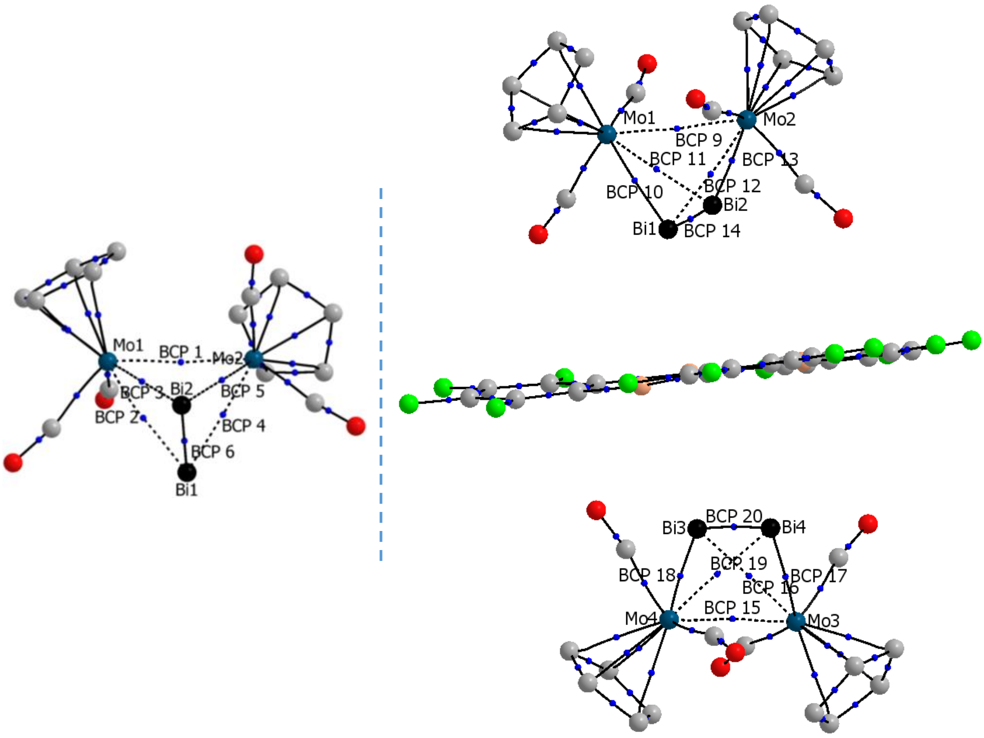

Figure 5. (Left) DFT-optimized electronic structure of **3d**. (Right) Electronic structure of [(**1**)•(**3d**)$_2$] at the observed crystal geometry. Bond critical points located *via* QTAIM analysis are shown as blue dots, with selected bond critical points of the Mo_2Bi_2 fragments labeled. Hydrogen atoms and bond critical points featuring ρ(r) values less than 0.006 e Å^{-3} are their corresponding bond paths are omitted for clarity.

Table 7. Features of the electron density distribution function (ρ(r)) at selected bond critical points of the Mo_2Bi_2 fragments in the structures of **3d** (white) and [(**1**)•(**3d**)$_2$] (grey).

BCP no. (A-B)	$d_{A\text{-}BCP}$ (Å)	$d_{B\text{-}BCP}$ (Å)	$\rho(r_{BCP})$ (e Å^{-3})	$\nabla^2\rho(r_{BCP})$ (e Å^{-5})	H_{BCP} (Hartree Å^{-3})	ε	δ(A,B)	$\oint_{A\cap B}\rho(r)$ (e Å^{-1})
1 (Mo1-Mo2)	1.610	1.610	0.208	0.30	-0.04	0.06	0.41	N/A[a]
2 (Mo1-Bi1)	1.476	1.542	0.278	0.68	-0.06	0.10	0.57	1.15
3 (Mo1-Bi2)	1.404	1.502	0.337	0.79	-0.09	0.23	0.76	1.21
4 (Mo2-Bi1)	1.404	1.502	0.337	0.79	-0.09	0.23	0.76	1.21
5 (Mo2-Bi2)	1.477	1.542	0.278	0.68	-0.06	0.10	0.57	1.15
6 (Bi1-Bi2)	1.426	1.426	0.381	1.09	-0.10	0.20	1.20	1.27
9 (Mo1-Mo2)	1.574	1.575	0.231	0.36	-0.05	0.07	0.42	N/A[a]
10 (Mo1-Bi1)	1.376	1.475	0.362	0.97	-0.10	0.23	0.73	1.26
11 (Mo1-Bi2)	1.445	1.510	0.307	0.77	-0.08	0.05	0.58	1.25
12 (Mo2-Bi1)	1.442	1.512	0.305	0.78	-0.08	0.01	0.56	1.25
13 (Mo2-Bi2)	1.378	1.472	0.365	0.94	-0.10	0.24	0.74	1.28
14 (Bi1-Bi2)	1.425	1.424	0.379	1.20	-0.10	0.25	1.08	1.32
15 (Mo3-Mo4)	1.573	1.568	0.233	0.37	-0.05	0.08	0.42	N/A[a]
16 (Mo3-Bi3)	1.437	1.510	0.307	0.81	-0.08	0.08	0.56	1.25
17 (Mo3-Bi4)	1.381	1.470	0.365	0.94	-0.10	0.22	0.75	1.31
18 (Mo4-Bi3)	1.381	1.482	0.356	0.93	-0.10	0.24	0.71	1.25
19 (Mo4-Bi4)	1.444	1.514	0.303	0.79	-0.07	0.05	0.57	1.27
20 (Bi3-Bi4)	1.427	1.427	0.375	1.20	-0.10	0.26	1.09	1.33

a: Due to the necessity to integrate the relevant atomic basins using the 'Promega' algorithm in AIMAll, the $\oint_{A\cap B}\rho(r_{BCP})$ value could not be determined.

3.3 Evaluation of intermolecular interactions in Mo_2E_2 adducts of 1 by QTAIM analysis

For all adducts of the Mo_2E_2 complexes with **1** presented, QTAIM analysis finds multiple intermolecular BCPs between the Hg and C atoms of **1** and the E or O atoms of **3a-d** (Figure 6-Figure 10).

Inspection of the values of ρ(r) at the E-Hg BCP for the adducts featuring end-on coordination of the Mo_2E_2 unit ([(**1**)•(**3a**)], [(**1**)•(**3b**)], and [$(\mathbf{1})_2$•(**3c**)]) finds that on average they decrease modestly as the identity of E is changed from P ($\rho(r_{BCP})$: 0.141-0.093 e $Å^{-3}$) to As ($\rho(r_{BCP})$: 0.127-0.101 e $Å^{-3}$) to Sb ($\rho(r_{BCP})$: 0.091 e $Å^{-3}$) (Table 8-Table 10). These values are in line with those previously reported for adducts of *cyclo*-P_5 and *cyclo*-As_5 ligands with **1**. The trend in ρ(r) values of the E-Hg BCPs in ([(**1**)•(**3a**)], [(**1**)•(**3b**)], and [$(\mathbf{1})_2$•(**3c**)]) is corroborated by the values of the E-Hg delocalization indices (δ(E,Hg)),[24] which correspond to the number of electron pairs delocalized between the two atoms, as well as the values obtained by integration of ρ(r) across the E-Hg interatomic surfaces ($\oint_{E\cap Hg}\rho(r)$). Taken together, these metrics suggest that the strength of the E-Hg interaction decreases in the order P>As>Sb, consistent with the donor strength trends typically observed for trivalent Group 15 ligands. While the values of δ(E,Hg) and $\oint_{E\cap Hg}\rho(r)$ suggest that the E-Hg interactions in these adducts possess a degree of covalency, the near-zero values of the total energy density at the BCP (H_{BCP}) found in all cases suggests that the E-Hg interactions are dominated by electrostatic and dispersion forces.[25]

For adducts [(**1**)•(**3c**)], and [(**1**)•$(\mathbf{3d})_2$] featuring Mo_2E_2 units coordinated in a side-on fashion, inspection of the features of ρ(r) at the E-Hg BCPs finds the E-Hg interactions to be similarly weak to those found in the end-on coordinated adducts (Table 11-Table 12). The values of $\rho(r_{BCP})$ found for the Mo_2Sb_2 adduct ($\rho(r_{BCP})$: 0.111-0.056 e $Å^{-3}$) are modestly larger than those found for the Mo_2Bi_2 adduct ($\rho(r_{BCP})$: 0.102-0.043 e $Å^{-3}$), which is again consistent with the typical Group 15 donor strength trends. This trend is again corroborated by the values of δ(E,Hg) and $\oint_{E\cap Hg}\rho(r)$ obtained. As with the end-on adducts, the values of H_{BCP} found for the E-Hg interactions are uniformly near-zero, again suggesting that the E-Hg interactions in these adducts are dominated by electrostatic and dispersion forces.

Comparing the features of ρ(r) obtained for the E-Hg interactions in the end-on Mo_2Sb adduct [$(\mathbf{1})_2$•(**3c**)] *versus* the side-on adduct [(**1**)•(**3c**)] finds that while the side-on adduct features stronger individual Sb-Hg interactions as evidenced by modestly elevated $\rho(r_{BCP})$, δ(E,Hg), and $\oint_{E\cap Hg}\rho(r)$ values, the strengths of the Sb-Hg interactions are on average similar across the two adducts. The most notable difference in the features of ρ(r) at the Sb-Hg BCPs between the end-on and side on Mo_2Sb_2 adducts are the values of the bond ellipticity (ε), which provide information on the anisotropy of the electron density relative to the bond path. For the end-on Mo_2Sb_2 adduct [$(\mathbf{1})_2$•(**3c**)], the ellipticity values at the Sb-Hg BCPs are 0.10, indicating only slight deviation of electron density from the bond path. In contrast, the three Sb-Hg BCPs found for [(**1**)•(**3c**)] feature ellipticity values of 0.01 (Sb1-Hg1), 0.15 (Sb1-Hg2), and 0.55 (Sb2-Hg3). The elevated values of ellipticity found for the latter two BCPs, particularly the Sb2-Hg3 BCP, suggest that electron density is anisotropically distributed about the BCP. This may suggest the involvement of an Sb-Sb bond in the interaction of **3c** with **1**. Similar elevated values of ellipticity (Bi1-Hg3: 0.29, Bi2-Hg2: 0.30, Bi3-Hg1: 1.08, Bi4-Hg3: 0.46) are found for the Bi-Hg BCPS in [(**1**)•$(\mathbf{3d})_2$], suggesting that the Bi-Bi bond of **3d** is involved in the Bi-Hg interactions observed in [(**1**)•$(\mathbf{3d})_2$].

Finally, it is important to note the role that intermolecular interactions between oxygen atoms of the carbonyl ligands in **3a**-**d** and the Hg and C atoms of **1**. Such interactions were found by QTAIM analysis in all adducts investigated. While the strength of these interactions ($\rho(r_{BCP})$: 0.043-0.079 e $Å^{-3}$) is in most cases weaker than that of the E-Hg interactions, they undoubtedly play a part in the observed aggregation modes.

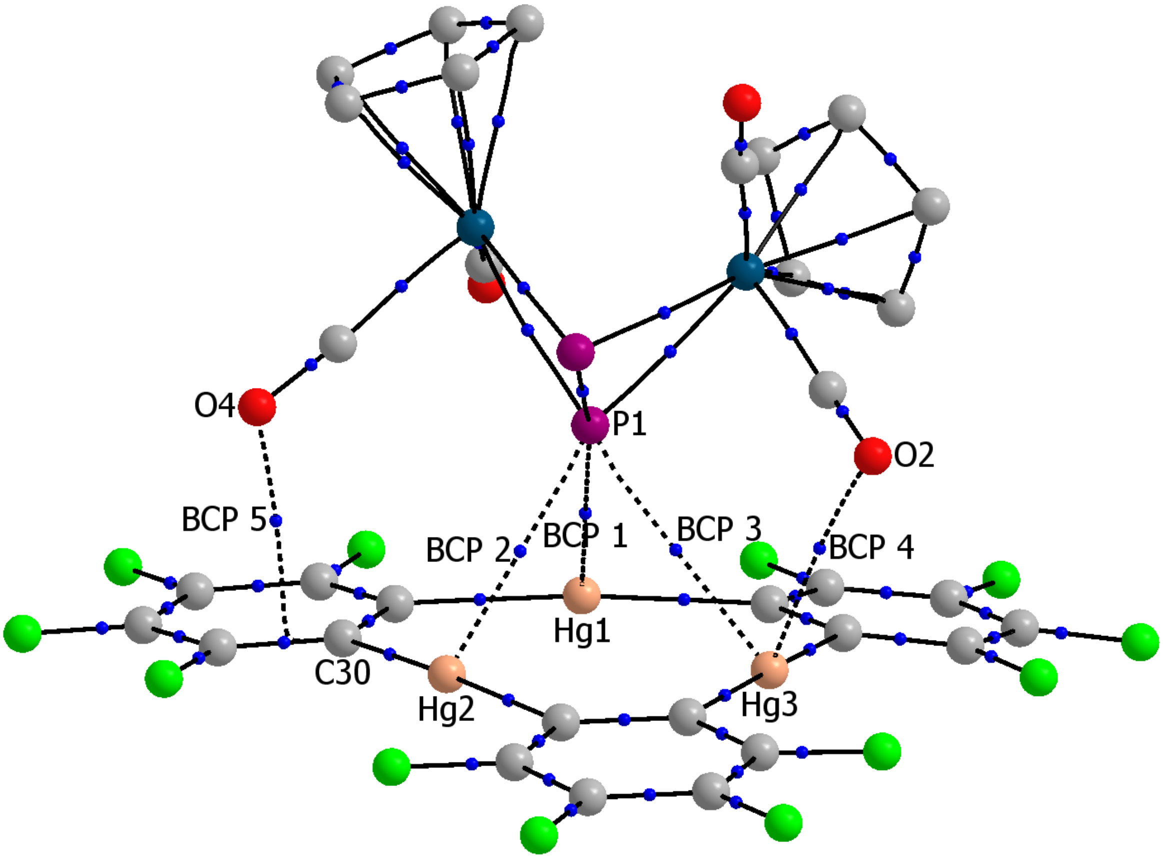

Figure 6. Electronic structure of [(**1**)•(**3a**)] at the observed crystal geometry. Bond critical points located *via* QTAIM analysis are shown as blue dots, with selected intermolecular bond critical points labeled. Hydrogen atoms and bond critical points featuring ρ(r) values less than 0.006 e Å^{-3} are their corresponding bond paths are omitted for clarity.

Table 8. Features of the electron density distribution function (ρ(r)) at selected intermolecular bond critical points in the structure of [(**1**)•(**3a**)].

BCP no. (A-B)	$d_{A\text{-}BCP}$ (Å)	$d_{B\text{-}BCP}$ (Å)	$\rho(r_{BCP})$ (e Å^{-3})	$\nabla^2\rho(r_{BCP})$ (e Å^{-5})	H_{BCP} (Hartree Å^{-3})	ε	δ(A,B)	$\oint_{A\cap B}\rho(r)$ (e Å^{-1})
1 (P1-Hg1)	1.581	1.581	0.141	1.13	-0.003	0.02	0.19	0.45
2 (P1-Hg2)	1.618	1.612	0.126	1.00	-0.001	0.08	0.17	0.46
3 (P1-Hg3)	1.669	1.690	0.093	0.80	0.003	0.07	0.12	0.31
4 (O2-Hg3)	1.539	1.809	0.051	0.61	0.01	0.59	0.04	0.21
5 (O4-C30)	1.503	1.687	0.052	0.64	0.01	3.31	0.03	0.23

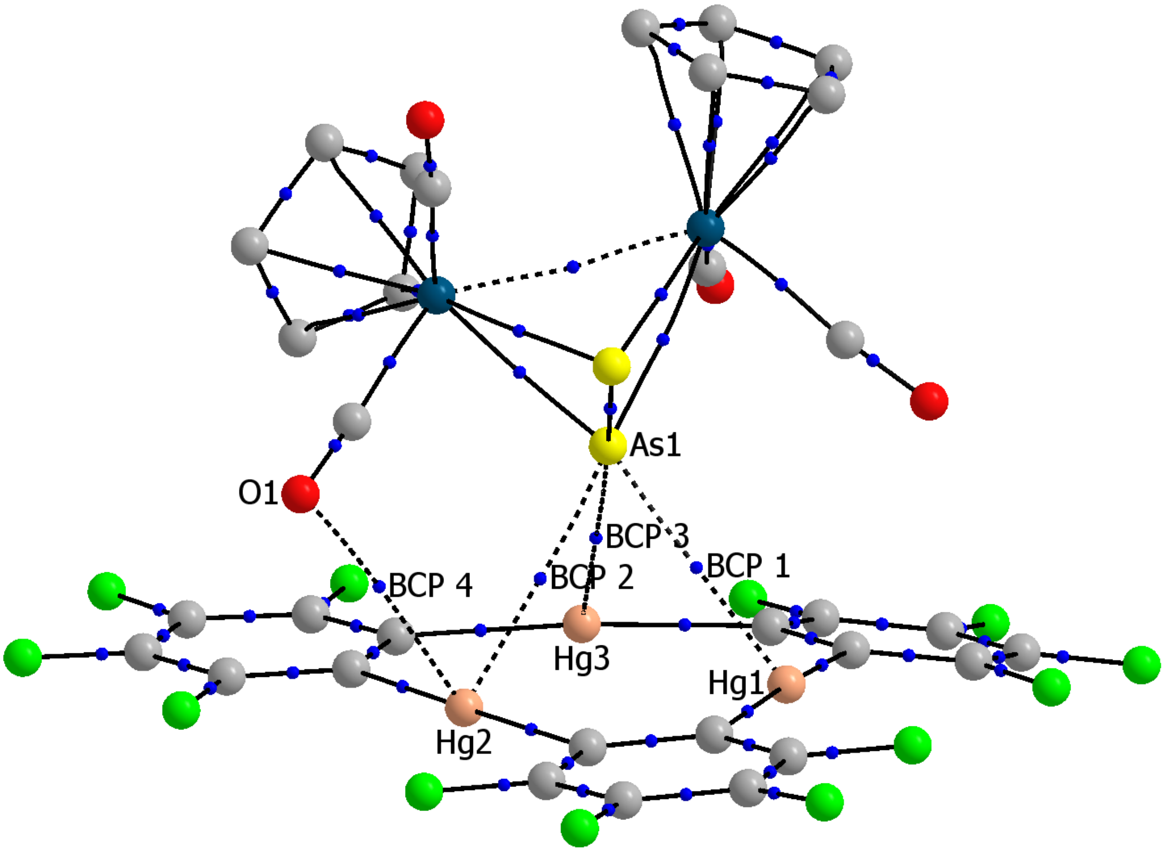

Figure 7. (Left) DFT-optimized electronic structure of **3b**. (Right) Electronic structure of [(**1**)•(**3b**)] at the observed crystal geometry. Bond critical points located *via* QTAIM analysis are shown as blue dots, with selected intermolecular bond critical points labeled. Hydrogen atoms and bond critical points featuring ρ(r) values less than 0.006 e Å^{-3} are their corresponding bond paths are omitted for clarity.

Table 9. Features of the electron density distribution function (ρ(r)) at selected intermolecular bond critical points in the structure of [(**1**)•(**3b**)].

BCP no. (A-B)	$d_{A\text{-}BCP}$ (Å)	$d_{B\text{-}BCP}$ (Å)	$\rho(r_{BCP})$ (e Å^{-3})	$\nabla^2\rho(r_{BCP})$ (e Å^{-5})	H_{BCP} (Hartree Å^{-3})	ε	δ(A,B)	$\oint_{A\cap B}\rho(r)$ (e Å^{-1})
1 (As1-Hg1)	1.652	1.619	0.127	0.94	-0.002	0.05	0.18	0.45
2 (As1-Hg2)	1.657	1.671	0.105	0.83	0.001	0.03	0.14	N/A^{a}
3 (As1-Hg3)	1.706	1.674	0.101	0.80	0.002	0.05	0.14	0.41
4 (O1-Hg2)	1.547	1.811	0.048	0.58	0.01	0.28	0.04	0.16

a: Due to the necessity to integrate the relevant atomic basins using the ‘Promega’ algorithm in AIMAll, the $\oint_{A\cap B}\rho(r_{BCP})$ value could not be determined.

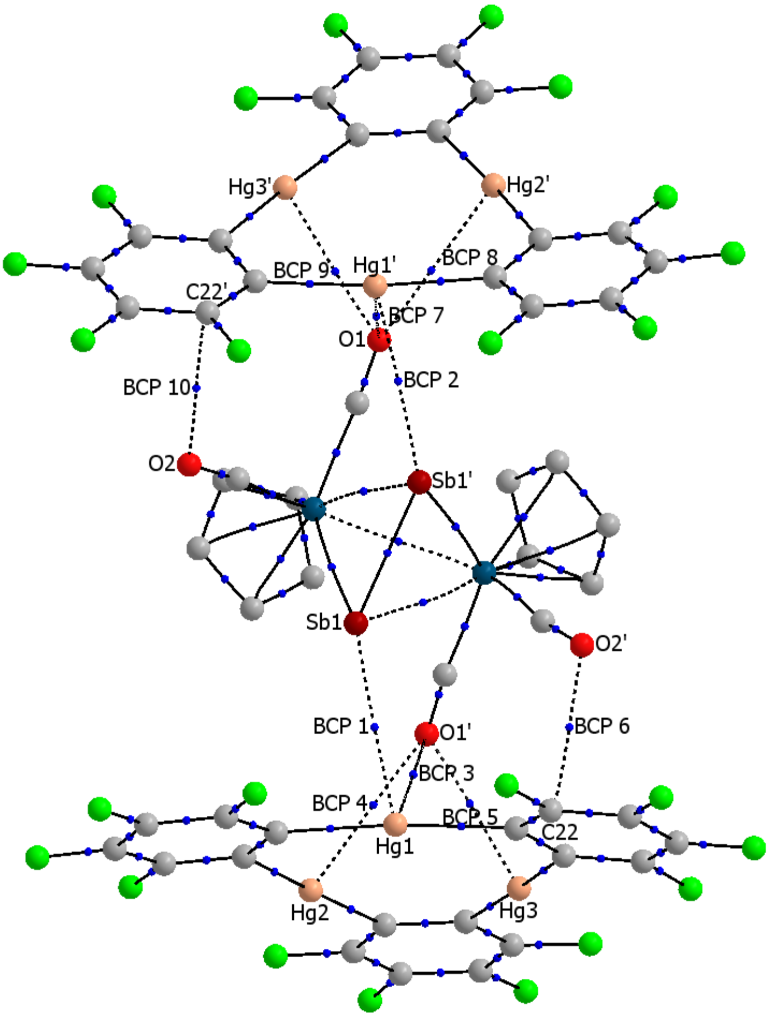

Figure 8. Electronic structure of [($\mathbf{1}$)$_2$•($\mathbf{3c}$)] at the observed crystal geometry. Bond critical points located *via* QTAIM analysis are shown as blue dots, with selected intermolecular bond critical points labeled. Hydrogen atoms and bond critical points featuring ρ(r) values less than 0.006 e Å^{-3} are their corresponding bond paths are omitted for clarity.

Table 10. Features of the electron density distribution function (ρ(r)) at selected intermolecular bond critical points in the structure of [($\mathbf{1}$)$_2$•($\mathbf{3c}$)].

BCP no. (A-B)	$d_{A\text{-}BCP}$ (Å)	$d_{B\text{-}BCP}$ (Å)	$\rho(r_{BCP})$ (e Å^{-3})	$\nabla^2 \rho(r_{BCP})$ (e Å^{-5})	H_{BCP} (Hartree Å^{-3})	ε	δ(A,B)	$\oint_{A\cap B}\rho$(r) (e Å^{-1})
1 (Sb1-Hg1)	1.816	1.713	0.091	0.67	0.002	0.10	0.14	0.42
2 (Sb1'-Hg1')	1.816	1.713	0.091	0.67	0.002	0.10	0.14	0.42
3 (O1'-Hg1)	1.480	1.753	0.063	0.73	0.004	0.04	0.06	0.17
4 (O1'-Hg2)	1.528	1.837	0.043	0.55	0.01	0.02	0.04	0.11
5 (O1'-Hg3)	1.409	1.683	0.079	0.95	0.01	0.04	0.08	0.22
6 (O2'-C22)	1.463	1.534	0.059	0.74	0.01	0.48	0.03	0.23
7 (O1-Hg1')	1.480	1.753	0.063	0.73	0.00	0.04	0.06	N/A^{a}
8 (O1-Hg2')	1.528	1.837	0.043	0.55	0.01	0.02	0.04	0.11
9 (O1-Hg3')	1.409	1.683	0.079	0.95	0.01	0.04	0.08	0.22
10 (O2-C22')	1.463	1.534	0.059	0.74	0.01	0.48	0.03	0.23

a: Due to the necessity to integrate the relevant atomic basins using the 'Promega' algorithm in AIMAll, the $\oint_{A\cap B}\rho(r_{BCP})$ value could not be determined.

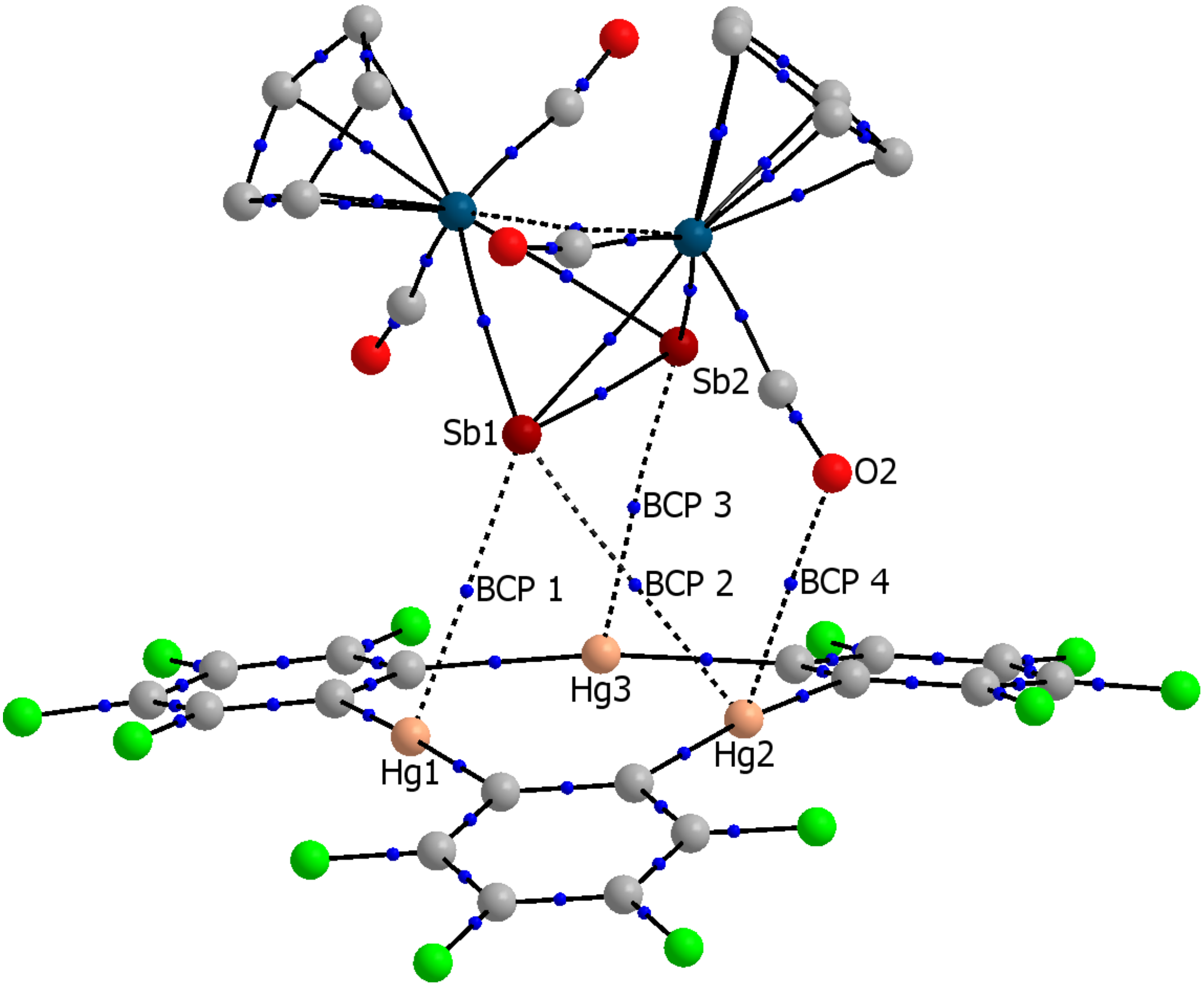

Figure 9. Electronic structure of [(**1**)•(**3c**)] at the observed crystal geometry. Bond critical points located *via* QTAIM analysis are shown as blue dots, with selected intermolecular bond critical points labeled. Hydrogen atoms and bond critical points featuring $\rho(\mathrm{r})$ values less than 0.006 e Å^{-3} are their corresponding bond paths are omitted for clarity.

Table 11. Features of the electron density distribution function ($\rho(\mathrm{r})$) at selected intermolecular bond critical points in the structures of [(**1**)•(**3c**)].

BCP no. (A-B)	$d_{A\text{-}BCP}$ (Å)	$d_{B\text{-}BCP}$ (Å)	$\rho(r_{BCP})$ (e Å^{-3})	$\nabla^2 \rho(r_{BCP})$ (e Å^{-5})	H_{BCP} (Hartree Å^{-3})	ε	δ(A,B)	$\oint_{A\cap B}\rho(r)$ (e Å^{-1})
1 (Sb1-Hg1)	1.769	1.665	0.111	0.79	0.000	0.01	0.18	0.42
2 (Sb1-Hg2)	2.012	1.853	0.056	0.40	0.003	0.15	0.08	0.18
3 (Sb2-Hg3)	1.824	1.705	0.100	0.68	0.001	0.55	0.16	0.61
4 (O2-Hg2)	1.425	1.696	0.073	0.87	0.01	0.07	0.07	0.22

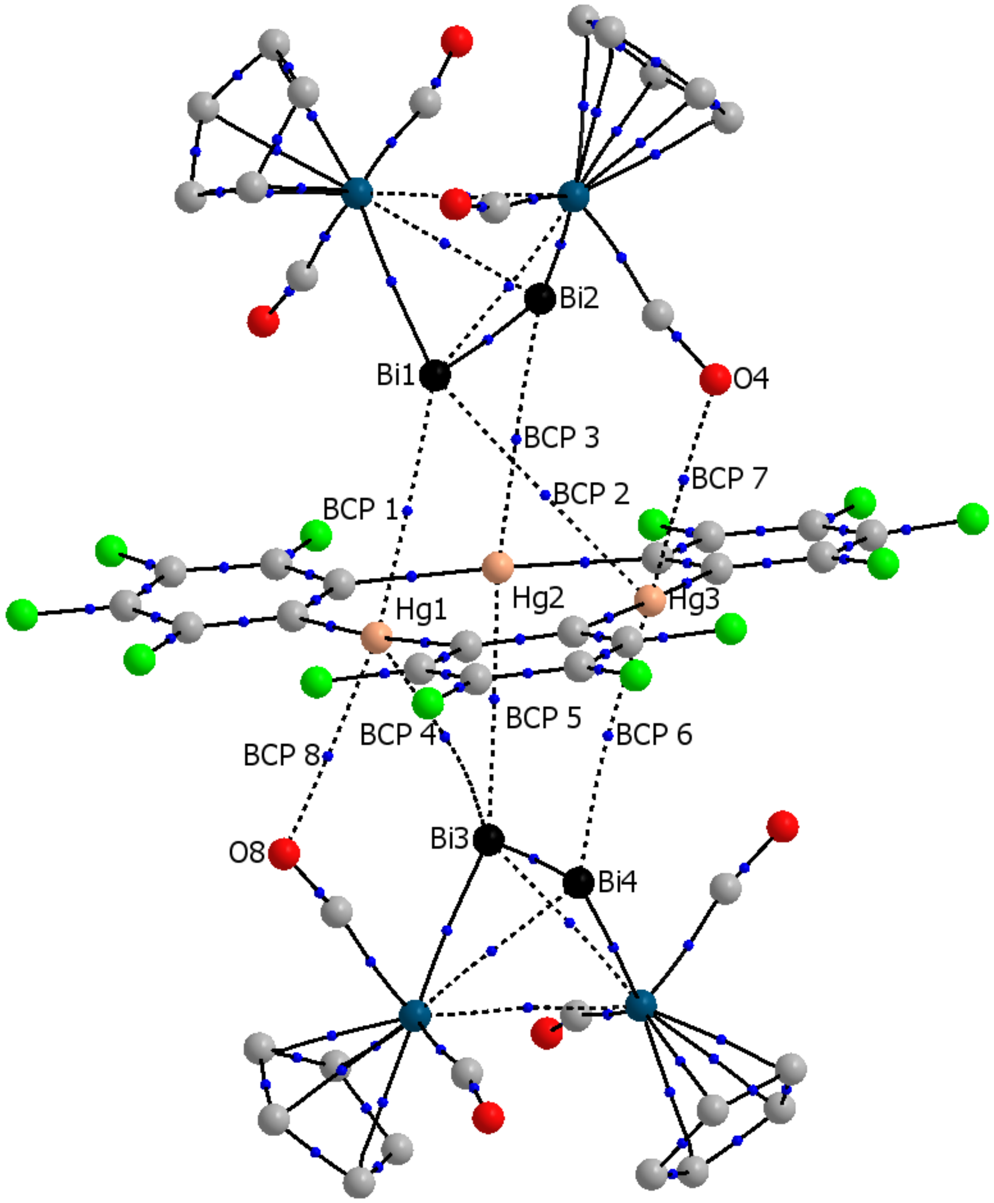

Figure 10. Electronic structure of [(**1**)•(**3d**)$_2$] at the observed crystal geometry. Bond critical points located *via* QTAIM analysis are shown as blue dots, with selected intermolecular bond critical points labeled. Hydrogen atoms and bond critical points featuring ρ(r) values less than 0.006 e Å^{-3} are their corresponding bond paths are omitted for clarity.

Table 12. Features of the electron density distribution function (ρ(r)) at selected intermolecular bond critical points in the structure of [(**1**)•(**3d**)$_2$].

BCP no. (A-B)	$d_{A\text{-}BCP}$ (Å)	$d_{B\text{-}BCP}$ (Å)	$\rho(r_{BCP})$ (e Å^{-3})	$\nabla^2\rho(r_{BCP})$ (e Å^{-5})	H_{BCP} (Hartree Å^{-3})	ε	δ(A,B)	$\oint_{A\cap B}\rho(r)$ (e Å^{-1})
1 (Bi1-Hg1)	1.794	1.692	0.102	0.77	0.001	0.01	0.16	0.43
2 (Bi1-Hg3)	2.121	1.931	0.043	0.32	0.003	0.29	0.06	0.13
3 (Bi2-Hg2)	1.888	1.754	0.085	0.58	0.002	0.30	0.14	0.49
4 (Bi3-Hg1)	2.045	1.886	0.054	0.37	0.003	1.08	0.07	0.25
5 (Bi3-Hg2)	1.855	1.734	0.088	0.65	0.002	0.05	0.14	0.38
6 (Bi4-Hg3)	1.948	1.840	0.064	0.47	0.003	0.46	0.10	0.43
7 (O4-Hg3)	1.466	1.740	0.063	0.74	0.01	0.08	0.06	0.20
8 (O8-Hg1)	1.413	1.683	0.078	0.92	0.00	0.05	0.08	0.27

References

[1] P. Sartori, A. Golloch, *Chem. Ber.* **1968**, *101*, 2004-2009.

[2] O. J. Scherer, H. Sitzmann, G. Wolmershäuser, *J. Organomet. Chem.* **1984**, *268*, C9-C12.

[3] J. R. Harper, A. L. Rheingold, *J. Organomet. Chem.* **1990**, *390*, C36-C38.

[4] P. J. Sullivan, A. L. Rheingold, *Organometallics* **1982**, *1*, 1547-1549.

[5] W. Clegg, N. A. Compton, R. J. Errington, G. A. Fisher, N. C. Norman, T. B. Marder, *J. Chem. Soc., Dalton Trans.* **1991**, 2887-2895.

[6] G. Balázs, H. J. Breunig, E. Lork, W. Offermann, *Organometallics* **2001**, *20*, 2666-2668.

[7] K. F. Wong, S. Ng, *Spectrochimica Acta Part A: Molecular Spectroscopy* **1976**, *32*, 455-456.

[8] G. M. Sheldrick, *Acta Cryst. A* **2008**, *64*, 112-122.

[9] O. V. Dolomanov, L. J. Bourhis, R. J. Gildea, J. A. K. Howard, H. Puschmann, *J. Appl. Crystallogr.* **2009**, *42*, 339-341.

[10] A. D. Becke, *J. Chem. Phys.* **1993**, *98*, 5648-5652.

[11] R. A. Kendall, T.H. Dunning, R. J. Harrison, *J. Chem. Phys.* **1992**, *96*, 6796-6806.

[12] K. A. Peterson, *J. Chem. Phys.* **2003**, *119*, 11099-11112.

[13] B. Metz, H. Stoll, M. Dolg, *J. Chem. Phys.* **2000**, *113*, 2563-2569.

[14] R. F. W. Bader, *Atoms in Molecules: A Quantum Theory*, Cambridge University Press: Oxford, UK, **1991**.

[15] T. A. Keith, AIMAII (Version 16.01.09) **2016**, TK Gristmill Software.

[16] M. J. Frisch, G. W. Trucks, H. B. Schlegel, G. E. Scuseria, M. A. Robb, J. R. Cheeseman, G. Scalmani, V. Barone, B. Mennucci, G. A. Petersson, H. Nakatsuji, M. Caricato, X. Li, H. P. Hratchian, A. F. Izmaylov, J. Bloino, G. Zheng, J. L. Sonnenberg, M. Hada, M. Ehara, K. Toyota, R. Fukuda, J. Hasegawa, M. Ishida, T. Nakajima, Y. Honda, O. Kitao, H. Nakai, T. Vreven, J. A. Montgomery Jr., J. E. Peralta, F. Ogliaro, M. J. Bearpark, J. Heyd, E. N. Brothers, K. N. Kudin, V. N. Staroverov, R. Kobayashi, J. Normand, K. Raghavachari, A. P. Rendell, J. C. Burant, S. S. Iyengar, J. Tomasi, M. Cossi, N. Rega, N. J. Millam, M. Klene, J. E. Knox, J. B. Cross, V. Bakken, C. Adamo, J. Jaramillo, R. Gomperts, R. E. Stratmann, O. Yazyev, A. J. Austin, R. Cammi, C. Pomelli, J. W. Ochterski, R. L. Martin, K. Morokuma, V. G. Zakrzewski, G. A. Voth, P. Salvador, J. J. Dannenberg, S. Dapprich, A. D. Daniels, Ö. Farkas, J. B. Foresman, J. V. Ortiz, J. Cioslowski, D. J. Fox, Gaussian, Inc., Wallingford, CT, USA, **2009**.

[17] a) G. A. Petersson, A. Bennett, T. G. Tensfeldt, M. A. Al-Laham, W. A. Shirley, J. Mantzaris, *J. Chem. Phys.* **1988**, *89*, 2193-2218; b) G. A. Petersson, M. A. Al-Laham, *J. Chem. Phys.* **1991**, *94*, 6081-6090; c) G. A. Petersson, T. G. Tensfeldt, J. A. Montgomery, *J. Chem. Phys.* **1991**, *94*, 6091-6101.

[18] K. A. Peterson, C. Puzzarini, *Theor Chem Acc* **2005**, *114*, 283-296.

[19] K. A. Peterson, D. Figgen, M. Dolg, H. Stoll, *J. Chem. Phys.* **2007**, *126*, 124101.

[20] D. Figgen, G. Rauhut, M. Dolg, H. Stoll, *Chem. Phys.* **2005**, *311*, 227-244.

[21] J. F. Van der Maelen, J. A. Cabeza, *Theor. Chem. Acc.* **2016**, *135*, 1-11.

[22] D. Tiana, E. Francisco, P. Macchi, A. Sironi, A. Martín Pendás, *J. Phys. Chem. A* **2015**, *119*, 2153-2160.

[23] L. J. Farrugia, P. Macchi, Bond Orders in Metal–Metal Interactions Through Electron Density Analysis. In *Electron Density and Chemical Bonding I: Experimental Charge Density Studies*; Stalke, D., Ed.; Springer Berlin Heidelberg: Berlin, Heidelberg, **2012**; pp 127-158.

[24] R. F. W. Bader, M. E. Stephens, *J. Am. Chem. Soc.* **1975**, *97*, 7391-7399.

[25] P. Macchi, A. Sironi, *Coord. Chem. Rev.* **2003**, *238–239*, 383-412.